

Observation of Townes solitons in two-dimensional Bose gases

Cheng-An Chen¹ and Chen-Lung Hung^{1,2,*}

¹ Department of Physics and Astronomy, Purdue University, West Lafayette, IN 47907 and

² Purdue Quantum Science and Engineering Institute, Purdue University, West Lafayette, IN 47907

(Dated: May 23, 2022)

New length scales often emerge in many-body systems driven out of equilibrium, leading to further development of delicate many-body states. Modulational instability, and the accompanying formation of solitons, is one important example. Here we report the observation of long-sought two-dimensional Townes solitons in atomic Bose gases quenched to attractive interactions. By monitoring the atomic density following interaction quenches, we observe instability-induced length scales that prevent samples from critical collapse and lead to surprisingly long-lived solitary waves. Our measurement reveals multiple universal behaviors derived from the energy scaling of modulational instability, including the quenched amplification of density waves, soliton formation, and their subsequent collision dynamics. Our work demonstrates new universal behavior in a non-equilibrium, scale-invariant many-body system, provides one viable approach in forming multidimensional solitons, and opens a window for studying these intricate self-bound many-body states.

Bright solitons are self-bound solutions to nonlinear wave equations [1]. Their existence and stability have been broadly discussed in physics across disciplines, from nonlinear optics [2, 3], matter waves [4–6] to cosmology [7, 8]. Fundamental solitons form at length scales where wave dispersion balances against nonlinear attraction. In two-dimensional (2D) Bose gases, however, scale invariance [9, 10] dictates that no prevailing length scale supports the formation of solitons [11]. One exception is the Townes soliton [12], which exists only around a critical atom number that scales with the coupling constant $g < 0$ as $N_{\text{th}} \approx 2\pi/|g|$ [11]. Once formed, a Townes soliton remains at any initial size. However, it is thought to be unstable against collapse or expansion for atom number either greater or smaller than N_{th} , making an experimental realization elusive.

It is known that breaking scale invariance helps stabilizing a 2D soliton at an associated length scale. For example, adding a harmonic trap [11] or lattice potential [13, 14] breaks translational invariance, permitting stable solitons below the Townes threshold and above a critical atom number. Introducing competing non-local interactions or scale-invariance breaking terms such as a dipolar interaction [15] or a spatiotemporal oscillating coupling constant [16, 17] can provide new length scales leading to stabilization.

Even without breaking scale invariance, a many-body system can pick up a new length scale being driven out of equilibrium. Examples include the sound horizon in a quenched superfluid [18] and the Kibble-Zurek mechanism [19, 20]. The prevailing non-equilibrium phenomenon in this study is modulational instability (MI) or dynamical instability [21, 22]. In atomic superfluids, when the repulsive interaction is suddenly quenched to attractive, collective modes with wavenumber $k_{\text{MI}} = \pi/\xi$ associated with the new interaction length scale $\xi =$

$\pi/\sqrt{2n_i|g|}$ (n_i being the initial number density) is expected to grow exponentially, becoming the dominating length scale that fragments a global wave function into pieces of wave packets [23, 24].

Intriguingly, the atom number in fragments $n_i \xi^2 \sim N_{\text{th}}$ scales critically with the Townes threshold in 2D (Fig. 1(A)). This simple relation applies universally for any n_i and $g < 0$ provided no new scales set in. One thus speculates if MI can assist the formation of long-lived Townes solitons, and if it can manifest against critical collapse and soliton collisions that further induce secondary collapse, as in the well-studied case of stable solitons in one-dimensional (1D) waveguides [25, 26].

In this paper, we report the observation of Townes solitons in quenched 2D Bose gases. We induce MI that can break up an otherwise large 2D sample into fragments universally around the Townes threshold, forming solitons that remain self-bound after long evolution time. Our measurement reveals universal solitary wave dynamics governed by the MI energy scale and a universal scaling behavior in the density power spectra, allowing us to clearly pinpoint a distinct time period for unstable growth of density waves, followed by a short era of wave collapse and soliton formation. By performing second interaction quenches, we further examine collapse and expansion time scales of this intricate many-body state.

For the quench experiments, we prepare 2D superfluids ($N \approx 1.5 \times 10^4$ cesium atoms) trapped inside a large quasi-2D box [27]. The atomic surface density is typically $n_i \approx 5 \times 10^8/\text{cm}^2$ within an area of $A \approx 60 \times 60 \mu\text{m}^2$ and with temperature $T \lesssim 5 \text{ nK}$. The tight vertical (z -) confinement of the box (Fig. 1(A)) freezes all atoms in the harmonic ground state along the z -axis. The initial interaction strength is tuned to $g_i = \sqrt{8\pi}a/l_z = 0.115$ via a magnetic Feshbach resonance [27], where a is the tunable s-wave scattering length and $l_z = 208 \text{ nm}$ is the vertical harmonic oscillator length.

We first induce MI by quenching the atomic interaction (in 1 ms) to a designated value $g_f < 0$. After a variable hold time τ , we perform absorption imaging to record the

* Email: clhung@purdue.edu

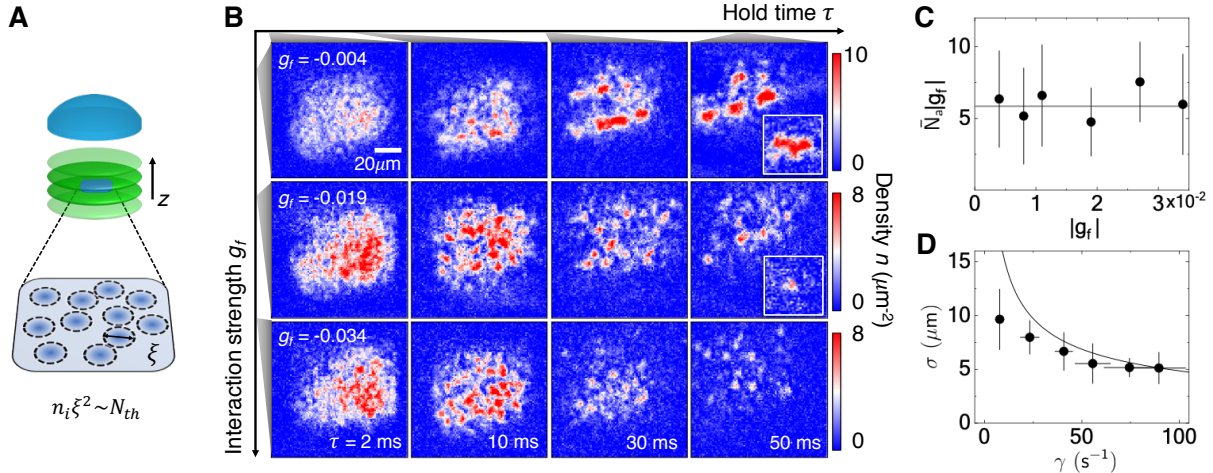


FIG. 1: Observation of Townes solitons in quenched 2D Bose gases. (A) Experimental scheme: A 2D gas of initial density n_i (blue shaded square) and interaction quenched to $g_f < 0$ is allowed to freely evolve for hold time τ in a horizontal plane defined by a single node of a repulsive standing-wave potential (green shaded ovals), and is imaged via a microscope objective (blue hemisphere) [27]. Quench-induced modulational instability fragments the sample into small wave packets of a characteristic size $\xi = \pi/\sqrt{2n_i|g_f|}$ (dashed circles). Atom number in each wave packet $\sim n_i \xi^2 = \pi^2/2|g_f|$ scales universally, for any n_i , around the precise Townes threshold $N_{th} = 5.85/|g_f|$ for 2D solitons [11]. (B) Shown in each row are single-shot images of samples quenched to the indicated g_f and held for the labeled time τ shown in each column. Solitons become visible at $\tau \gtrsim 30$ ms. Inset images are recorded at hold time $\tau = 2$ s ($g_f = -0.004$) and 1 s ($g_f = -0.019$), respectively (image size: $30 \times 30 \mu\text{m}^2$; density is scaled up by two times for viewing). (C) Scaled mean atom number in soliton $\bar{N}_a|g_f|$ versus $|g_f|$. Solid line marks the universal threshold $N_{th}|g_f| = 5.85$. (D) Mean soliton size σ (root-mean-square diameter) versus interaction energy $\hbar\gamma = \frac{\hbar^2 n_i |g_f|}{m}$, where m is the atomic mass and \hbar is the reduced Planck constant. Solid line is MI length ξ . All data points in (C-D) are evaluated at $\tau = 42 \sim 50$ ms except for $g_f = -0.004$ which are evaluated at $\tau = 150 \sim 200$ ms. All error bars are standard deviations.

sample density distribution. Typically around 30 experiment repetitions are performed for ensemble analyses. Figure 1(B) shows single-shot sample images following the interaction quench. At short hold time $\tau \lesssim 30$ ms, we observe that the atomic density clumps up into randomly distributed blobs throughout the sample. The characteristic sizes of the blobs are smaller with larger interaction $|g_f|$, consistent with MI observed in quasi-1D waveguides [25, 28]. At longer hold time $\tau \gtrsim 30$ ms, the number of blobs reduces, becoming more isolated, although their characteristic size and atom number evolve much slower or remain approximately constant for $\tau \leq 200$ ms [27]. We observe long-lived density blobs for hold time as long as 2 s; see Fig. 1(B) insets.

We identify these isolated blobs as Townes solitons and confirm MI-induced soliton formation. Taking the soliton density profile as approximately Gaussian [11], we perform 2D fits to determine their mean size σ and atom number \bar{N}_a at hold time $\tau > 40$ ms [27]. In Fig. 1(C), we plot the scaled atom number $\bar{N}_a|g_f|$ over a wide range of attractive interactions $-0.004 \geq g_f \geq -0.034$. We find that all scaled numbers fall around the Townes threshold, and give a mean value $\bar{N}_a|g_f| = 6(1)$. Interestingly, the standard deviation of the soliton atom number (δN_a) scales accordingly, giving a mean $\bar{\delta N}_a|g_f| = 3.2(5)$ with relatively small (16 %) deviation across all g_f . In Fig. 1(D), we show that the soliton size agrees well with the prediction $\sigma \approx \xi$, indicating that MI indeed provides

the critical length scale for forming Townes solitons.

Further evidences of MI-induced solitary wave dynamics manifest in the density power spectrum $S(k, \tau) = \frac{\langle |n(k, \tau)|^2 \rangle}{N}$ in spatial frequency domain, evaluated using Fourier transform of density $n(\mathbf{r})$ at hold time τ and azimuthal averaging at $k = |\mathbf{k}|$, N is the total atom number, and $\langle \cdot \rangle$ denotes ensemble averaging [18]. The density power spectra are analogous to the time frequency spectra for MI in nonlinear fibers [29] but with a monitor of dynamics also in the early stage. Figure 2(A) plots sample $S(k, \tau)$, demonstrating the initial growth ($\tau = 2 \sim 10$ ms) and decay ($\tau > 10$ ms) of density modulations at certain length scales.

To quantify the growth of density waves across all k -modes, we further plot the relative growth spectra $\tilde{S}(k, \tau) = \frac{S(k, \tau)}{S(k, \tau_0)}$, using the curve at $\tau_0 = 2$ ms as a reference. In each measurement presented in Figs. 2(B-C), we observe a broad peak developing in $\tilde{S}(k, \tau)$ within $0.2/\mu\text{m} < k < 1/\mu\text{m}$ and at short hold time $\tau < 20$ ms, signaling density waves growing in the sample. The broad peak then dissipates at longer hold time $\tau \gtrsim 20$ ms until $S(k, \tau)$ again becomes monotonic and stationary in momentum space, suggesting the collapse or break up of density waves. The growth patterns look similar for samples with different g_f , although the peak location, height, and the evolution time scale vary. In Fig. 2(D), we identify the peak wavenumber k_p for the

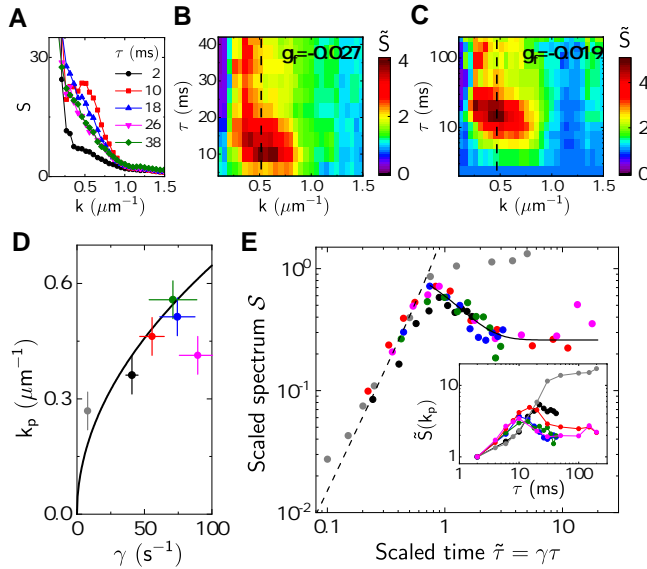


FIG. 2: Modulational instability and universal scaling in the density power spectra. (A) Sample spectra $S(k, \tau)$ at $g_f = -0.027$ and the indicated hold time τ . (B) Corresponding growth spectra $\tilde{S}(k, \tau) = S(k, \tau)/S(k, \tau_0)$ with $\tau_0 = 2$ ms. (C) Sample growth spectra \tilde{S} at $g_f = -0.019$ and hold time up to 200 ms. Vertical dashed lines in (B-C) mark the fastest growing wavenumber k_p . (D) k_p versus interaction energy unit γ (filled circles) measured at $g_f = -0.004$ (gray), -0.011 (black), -0.019 (red), -0.027 (blue), and -0.034 (magenta and olive), respectively. Corresponding $\tilde{S}(k_p, \tau)$ are shown in the inset of (E). Solid line is the prediction $k_{\text{MI}} = \sqrt{2\gamma m/\hbar}$. Error bars include systematic and statistical errors. (E) Scaled spectra S plotted using Eq. (1), which collapse approximately onto a single curve except for the one at $g_f = -0.004$. Dashed line (Solid line) is a hyperbolic (exponential) fit to the growth (decay) part of the curve; see text.

fastest growing mode. Our result is again consistent with the prediction $k_{\text{MI}} = \sqrt{2n_i|g_f|}$, which has the largest imaginary part in the Bogoliubov dispersion relation $\epsilon(k) = \frac{\hbar^2}{2m} \sqrt{|k^4 + 4n_i g_f k^2|} \leq \hbar\gamma$.

We focus on the peak spectra $\tilde{S}(k_p, \tau)$ and show that they further reveal a universal time and amplitude scaling behavior with respect to the interaction energy $\hbar\gamma$, summarized as the following [27]

$$S(\tilde{\tau}) = \frac{\gamma}{\tilde{\gamma}_i} [\tilde{S}(k_p, \tilde{\tau}) - 1]. \quad (1)$$

Here $\tilde{\tau} = \gamma\tau$ is the scaled time and $S(\tilde{\tau})$ is the scaled spectrum. In the amplitude scaling, we normalize γ with the mean initial interaction energy $\tilde{\gamma}_i = 306$ s⁻¹ of all samples before the quench. In Fig. 2 (E), we show that six power spectra, each measured with different energy $\hbar\gamma$, can collapse approximately onto a single curve using the scaling relation Eq. (1). The only exception is the spectrum with $g_f = -0.004$, where we have used $\gamma^* = 3.2\gamma$ to force its collapse within $\tilde{\tau} \lesssim 0.8$. This different behavior is likely the manifestation of poten-

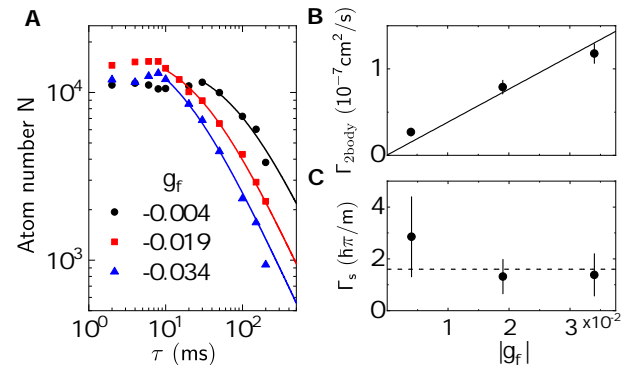


FIG. 3: Universal soliton collision dynamics in 2D. (A) Total atom number N versus hold time τ measured at the indicated g_f . Solid lines are two-body loss fits after atom loss initiates. (B) Fitted rate coefficients from (A). Solid line is a linear fit, giving a slope $\Gamma_{\text{2body}}/|g_f| = 3.9(6) \times 10^{-6}$ cm²/s. (C) 2D soliton binary loss coefficients Γ_s determined from the rate coefficients in (B) and \bar{N}_a in Fig. 1(C), and compared with the universal prediction $\Gamma_s = \eta\hbar\pi/m$, giving a mean $\eta = 1.9(7)$. Dashed line marks the constant $\eta = 1.6(4)$ alternatively determined from the fitted slope in (B) and mean $\bar{N}_a|g_f| = 6(1)$ [27]. Error bars are standard deviations.

tial corrugations in the vertical confining trap, as $\gamma/2\pi$ is merely 1.2 Hz in this sample.

From this approximate universal behavior, we identify two distinct regimes of quench dynamics, divided by a critical time $\tilde{\tau}_i \approx 0.8$. We label the time period $\tilde{\tau} \lesssim \tilde{\tau}_i$ for MI with an expected hyperbolic growth of density waves

$$\tilde{S}(k_p, \tau) \approx 1 + \alpha \frac{\tilde{\gamma}_i}{\gamma} \sinh^2(\gamma\tau), \quad (2)$$

where $\alpha = 1.5(1)$ is determined from a fit to $S(\tilde{\tau})$ for $\tilde{\tau} \leq 0.5$; $\alpha = 2$ is expected from a modified Bogoliubov theory without considering the depletion of ground state atoms [27]. Beyond $\tilde{\tau} \gtrsim \tilde{\tau}_i$ after $S(\tilde{\tau})$ reaches order of unity, the dynamics enters the second phase, decaying with a time constant $\Delta\tilde{\tau} \sim 0.8$ and transitioning to a slowly-evolving behavior. This indicates breaking up of density waves followed by soliton formation. For the sample $g_f = -0.004$, $\tilde{S}(k_p, \tau)$ remains slowly-growing within $1 \lesssim \gamma^*\tau \lesssim 10$, suggesting less severe wave collapse.

Following the observed universal density wave dynamics and soliton formation, we show that MI energy scale continues to manifest through soliton collision dynamics. When solitons of like-phases collide, merger can occur [14], leading to atom number $N_a > N_{\text{th}}$ and inducing secondary collapse that quickly removes the merged soliton. Intriguingly, MI scaling and 2D scale-invariance together suggest a universal binary loss coefficient in 2D [27]

$$\Gamma_s = \eta \frac{\hbar\pi}{m}, \quad (3)$$

because $\Gamma_s \sim \sigma\bar{v}$ and the scale dependencies in the soliton cross-section $\sigma \approx \xi$ and relative velocity $\bar{v} \approx \sqrt{2\hbar\pi/m\xi}$

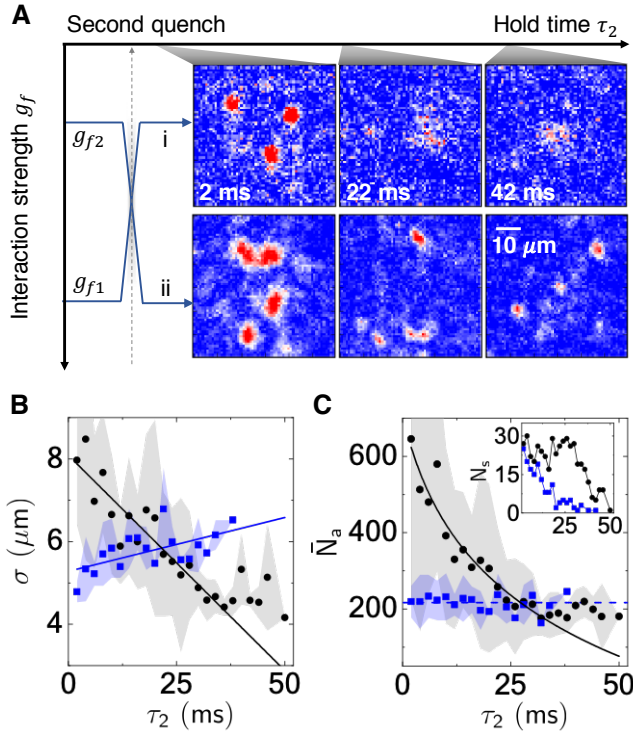


FIG. 4: Collapse and expansion dynamics following second interaction quenches. (A) Path i (ii): expansion (collapse) dynamics is initiated in solitons that are initially formed at $g_{f1} = -0.027$ (or $g_{f2} = -0.008$) followed by a second quench to g_{f2} (or g_{f1}). Single-shot sample images are recorded at the indicated hold time τ_2 after the second quench. (B) and (C), mean size σ and atom number \bar{N}_a versus τ_2 for paths i (blue squares) and ii (black circles), respectively. In (B), solid lines are linear fits, giving expansion and collapse rates $\dot{\sigma}$; see text. In (C), blue dashed line marks the Townes threshold $N_{th} = 5.85/|g_{f1}|$. Black solid line is a three-body loss fit [27]. Inset shows the observed soliton number N_s at each hold time τ_2 . Shaded bands represent standard deviations.

cancel each other exactly. A constant $\eta \approx \sqrt{2}$ considers $\sim 50\%$ probability for soliton merger. If this collision picture holds, we expect a collision lifetime $\frac{1}{n_s \Gamma_s} \sim \gamma^{-1}$ once solitons form, where $n_s = \frac{n_i}{\bar{N}_a}$ is the initial soliton density [27]. This suggests that wave collapse and binary collision loss likely take place simultaneously in the second phase of the density wave evolution $\tilde{\tau} \gtrsim \tilde{\tau}_i$.

In Fig. 3, we confirm the 2D collision scaling Eq. (3) by examining the total atom number loss in samples of different g_f . Each measurement displays an onset of loss starting from a time τ that corresponds to the critical time $\tilde{\tau}_i$ for the second phase of dynamics [25, 27]. We confirm that all loss curves can be well-captured by a simple two-body loss model, $\dot{N}/N = -\Gamma_{2\text{body}} N/A$, suggesting that soliton collisions induce the atom loss. The 2D binary loss coefficient can be deduced from the relation $\Gamma_s = \Gamma_{2\text{body}} \bar{N}_a$ [27]. In Fig. 3(B), we find that the measured $\Gamma_{2\text{body}}$ scales linearly with $|g_f|$, indeed suggesting a universal Γ_s since $\bar{N}_a |g_f| \approx 6$ is a universal

number. To unambiguously confirm the collision universality, in Fig. 3(C) we further deduce Γ_s independently using experimentally determined values ($\Gamma_{2\text{body}}, \bar{N}_a$) at each g_f . Our results conform very well with the prediction by Eq. (3). The observations in Figs. 2 and 3 together confirm that Townes solitons form at $\tau \gtrsim \gamma^{-1}$, followed by collision (and collapse) also at the same time scale γ^{-1} universally governed by MI.

To further gain insight into the stability of surviving Townes solitons, we now determine their collapse (expansion) time scales by driving the atom number away from the Townes threshold. To do this, we apply second interaction quench after solitons have formed at $\tau = 50$ ms, followed by additional hold time τ_2 and imaging to determine \bar{N}_a and σ of the surviving solitons. In a quench-up experiment labeled as path i in Fig. 4, we quench to an interaction that is over three times less attractive. We immediately observe soliton expansion until $\tau_2 > 40$ ms when image noise prevents us from obtaining reliable measurements. During the expansion, \bar{N}_a remains constant but the number of solitons N_s observed from the ensemble of measurements greatly reduces (Fig. 4(C) and inset).

For a reversed quench-down experiment (path ii), solitons collapse due to three times smaller Townes threshold than initial \bar{N}_a . We observe rapid reductions in both σ and \bar{N}_a . The atom loss within a soliton is presumably due to three-body recombination. In Fig. 4(C), we determine a three-body loss coefficient $L_3 = 1.1(1) \times 10^{-23} \text{ cm}^6/\text{s}$ that is five orders of magnitude larger than those measured in 3D thermal samples [27]. Interestingly, the collapse seemingly slows down as \bar{N}_a drops to the new threshold value at around $\tau_2 \geq 36$ ms. This suggests either three-body loss has regulated the collapse, or only solitons with initial N_a close to the new threshold survives. The observed sudden loss of N_s beyond $\tau_2 \geq 36$ ms (Fig. 4(C) inset) may suggest the latter case.

In either quench paths, soliton evolution is clearly visible within the interaction time scale. The collapse (expansion) rate is $\dot{\sigma} \approx -1.8 \gamma' \mu\text{m}$ ($0.5 \gamma' \mu\text{m}$) for the quench-down (quench-up) experiment, where $\gamma' = \hbar \bar{n} |g_{f2} - g_{f1}|/m \approx 55 \text{ s}^{-1}$ is the interaction energy difference and $\bar{n} \approx 6/\mu\text{m}^2$ is soliton initial peak density. Such rapid evolution is not observed in solitons formed after a single quench and at long hold time $\tau > 50$ ms [27]. Given the large spread of $\delta N_a / \bar{N}_a \approx 0.5$ observed in Fig. 1 (C), it remains speculative if additional length scales, such as imperfect trap corrugation, could have set in to further slow down soliton dynamics.

In conclusion, we report universal formation of Townes solitons in 2D Bose gases quenched to attractive interactions. Our work offers a new example on dynamical formation of an intricate many-body state that is difficult to form in equilibrium, imposing also additional questions such as the role of coherence in MI and its dependence on the initial states prior to a quantum quench. Our quench recipe may also be extended to form new many-body states such as vortex solitons [11, 30].

[1] A. Shabat and V. Zakharov, Soviet physics JETP **34**, 62 (1972).

[2] Y. S. Kivshar and G. Agrawal, *Optical solitons: from fibers to photonic crystals* (Academic press, 2003).

[3] Z. Chen, M. Segev, and D. N. Christodoulides, Reports on Progress in Physics **75**, 086401 (2012).

[4] K. E. Strecker, G. B. Partridge, A. G. Truscott, and R. G. Hulet, Nature **417**, 150 (2002).

[5] L. Khaykovich, F. Schreck, G. Ferrari, T. Bourdel, J. Cubizolles, L. D. Carr, Y. Castin, and C. Salomon, Science **296**, 1290 (2002).

[6] S. L. Cornish, S. T. Thompson, and C. E. Wieman, Physical review letters **96**, 170401 (2006).

[7] T.-D. Lee and Y. Pang, Physics Reports **221**, 251 (1992).

[8] S. Khlebnikov and I. Tkachev, Physical Review D **61**, 083517 (2000).

[9] C.-L. Hung, X. Zhang, N. Gemelke, and C. Chin, Nature **470**, 236 (2011), ISSN 0028-0836.

[10] T. Yefsah, R. Desbuquois, L. Chomaz, K. J. Günter, and J. Dalibard, Physical review letters **107**, 130401 (2011).

[11] B. A. Malomed, The European Physical Journal Special Topics **225**, 2507 (2016).

[12] R. Y. Chiao, E. Garmire, and C. H. Townes, Physical review letters **13**, 479 (1964).

[13] N. K. Efremidis, J. Hudock, D. N. Christodoulides, J. W. Fleischer, O. Cohen, and M. Segev, Physical review letters **91**, 213906 (2003).

[14] B. B. Baizakov, B. A. Malomed, and M. Salerno, Physical Review A **70**, 053613 (2004).

[15] P. Pedri and L. Santos, Physical review letters **95**, 200404 (2005).

[16] H. Saito and M. Ueda, Physical review letters **90**, 040403 (2003).

[17] Y. V. Kartashov, B. A. Malomed, and L. Torner, Reviews of Modern Physics **83**, 247 (2011).

[18] C.-L. Hung, V. Gurarie, and C. Chin, Science **341**, 1213 (2013), ISSN 0036-8075.

[19] T. W. Kibble, Physics Reports **67**, 183 (1980).

[20] W. H. Zurek, Nature **317**, 505 (1985).

[21] P. Kevrekidis and D. Frantzeskakis, Modern Physics Letters B **18**, 173 (2004).

[22] V. E. Zakharov and L. Ostrovsky, Physica D: Nonlinear Phenomena **238**, 540 (2009).

[23] L. Salasnich, A. Parola, and L. Reatto, Physical review letters **91**, 080405 (2003).

[24] L. D. Carr and J. Brand, Physical review letters **92**, 040401 (2004).

[25] J. H. Nguyen, D. Luo, and R. G. Hulet, Science **356**, 422 (2017).

[26] J. H. Nguyen, P. Dyke, D. Luo, B. A. Malomed, and R. G. Hulet, Nature Physics **10**, 918 (2014).

[27] *See supplementary materials.*

[28] P. Everitt, M. Sooriyabandara, M. Guasoni, P. Wigley, C. Wei, G. McDonald, K. Hardman, P. Manju, J. Close, C. Kuhn, et al., Physical Review A **96**, 041601 (2017).

[29] D. Solli, G. Herink, B. Jalali, and C. Ropers, Nature Photonics **6**, 463 (2012).

[30] L. Carr and C. W. Clark, Physical review letters **97**, 010403 (2006).

[31] C.-L. Hung, X. Zhang, N. Gemelke, and C. Chin, Physical Review A **78**, 011604 (2008).

[32] C. Chin, R. Grimm, P. Julienne, and E. Tiesinga, Reviews of Modern Physics **82**, 1225 (2010).

[33] T. Kraemer, M. Mark, P. Waldburger, J. G. Danzl, C. Chin, B. Engeser, A. D. Lange, K. Pilch, A. Jaakkola, H.-C. Nägerl, et al., Nature **440**, 315 (2006).

[34] M. Gustavsson, E. Haller, M. Mark, J. Danzl, G. Rojas-Kopeinig, and H.-C. Nägerl, Physical review letters **100**, 080404 (2008).

[35] D. Petrov, M. Holzmann, and G. Shlyapnikov, Physical Review Letters **84**, 2551 (2000).

[36] C.-L. Hung, X. Zhang, L.-C. Ha, S.-K. Tung, N. Gemelke, and C. Chin, New Journal of Physics **13**, 075019 (2011).

[37] L. Feng, L. W. Clark, A. Gaj, and C. Chin, Nature Physics **14**, 269 (2018).

[38] L. Pitaevskii and S. Stringari, *Bose-Einstein condensation and superfluidity*, vol. 164 (Oxford University Press, 2016).

Acknowledgments: We acknowledge discussions with Qi Zhou, Cheng Chin, Chih-Chun Chien, Sergei Khlebnikov, and Chris Greene. We are grateful to H. J. Kimble for instrument loan since the early stage of this project. We thank May Kim, Yiyang Fang, and Wuxiucheng Wang for laboratory assistance. This project is supported in part by the W. M. Keck Foundation, the NSF Award PHY-1848316, and the U.S. Department of Energy (grant# DE-SC0019202).

Appendix A: Supplementary Materials

Experimental procedures: preparation and detection of two-dimensional (2D) Bose gases in a quasi-2D box potential

The quasi-2D box potential. Figure S1 shows the schematics of the experiment. Our quench experiment begins with a nearly uniform 2D Bose gas confined in a quasi-2D box potential, which is formed by all repulsive optical dipole beams. The vertical box confinement is provided by a single node of a repulsive standing-wave potential ($2 \mu\text{m}$ periodicity) along the vertical (z)-direction. The node defines the horizontal 2D plane. The standing-wave potential is formed by the interference of two 780 nm vertical confinement beams crossing at the horizontal plane with 22 degree separation angle. The measured vertical trap frequency in the node is $\omega_z/2\pi = 1.75(2)$ kHz $\gg (k_B T, |\mu|)/\hbar$, thus freezing all atoms in the harmonic ground state. Here k_B is the Boltzmann constant, $T \lesssim 5$ nK is the temperature of the 2D gas and μ is the chemical potential. The horizontal boundary of the box is formed by a tightly focused 780 nm optical beam that scans the box boundary at a 15 kHz repetition rate to form a time-averaged, repulsive wall potential. The beam is controlled by a pair of acousto-optic deflector and is projected through a microscope objective (numerical aperture N.A. = 0.37). When the wall potential is removed, the residual global trap frequency in the horizontal plane, due to a weak magnetic trap, is experimentally determined to be $\omega_r/2\pi < 1.5$ Hz through induced superfluid dipole oscillations.

2D box loading procedure. To load a quantum gas into the 2D box potential, we first prepare $N \approx 1.5 \times 10^4$ nearly pure Bose-condensed cesium atoms (BEC) in the $|F = 3, m_F = 3\rangle$ hyperfine ground state [31]. The three-dimensional (3D) BEC is initially trapped in an oblate dipole trap formed by two crossed dipole beams and a horizontal sheet beam, all derived from a 1064 nm MOPA laser and frequency-shifted to avoid interference. The BEC is first evaporatively cooled at a background magnetic field at $B = 23.6$ G, corresponding to a scattering length of $a = 320 a_0$ (a_0 is the Bohr radius). Near the end of the evaporation, the magnetic field is jumped to 18.6 G to prepare the final BEC at a smaller scattering length at $a \approx 90 a_0$ for box loading. We then ramp on the box potential in 200 ms to compress the 3D BEC into a thin sheet of 2D superfluid, followed by a 100 ms ramp to turn off all other attractive 1064 nm dipole beams. The vertical alignment between the 3D BEC and the box potential has been carefully adjusted, and the single-node loading in the standing-wave potential is confirmed by nulling the matter-wave interference pattern along the vertical (z)-axis during time-of-flight, which is sensitive to small number of atoms present in the adjacent nodes. The sample temperature is measured to be $T < 8$ nK after being released back to the 3D oblate trap using a reversed process. Compared to the negligible thermal components before the box loading, this gives an estimate of $T \lesssim 5$ nK for our 2D samples in the box, which underwent compression along the z -axis but decompression in the horizontal plane.

Quench experiment procedure. Following the box loading, we initiate the interaction quench by jumping the background magnetic field in < 1 ms to a designated value near $B = 17$ G while simultaneously removing the wall potential, allowing hot collision products (due to soliton collapses) to eject out of the experiment field of view. After a variable hold time τ , we perform absorption imaging by illuminating the 2D sample with an intense resonant beam for 10 μs and use a charge-coupled device (CCD) camera to record the atomic shadow image through the microscope objective. Conversion to 2D density images follows that described in Ref. [9], derived using Beer's law

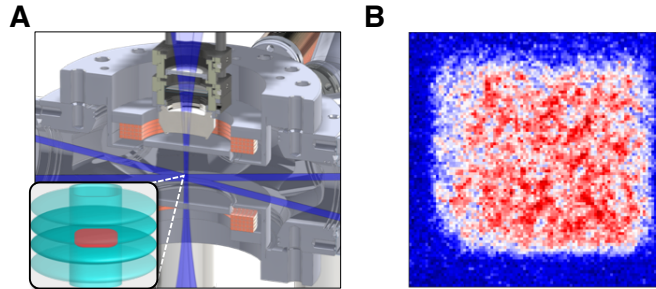


Fig. S1: (A) Schematic of the experiment showing two crossed vertical confinement beams (blue shaded sheets) and the wall beam (blue shaded cylinder). Inset illustrates a 2D gas (red shaded square) confined in the box potential, which is represented by a single node between the blue shaded ovals with the square-wall cylinder beam forming the box boundary. (B) Single-shot sample image of a 2D gas loaded in the box potential. Image size is $90 \times 90 \mu\text{m}^2$ and pixel size is $1 \mu\text{m}^2$.

and a calibrated atom-photon cross-section. For this experiment, image magnification is chosen such that the CCD pixel size corresponds to $1 \mu\text{m}^2$ in the object plane. We characterize the image resolution $< 2 \mu\text{m}$ by focusing on the smallest solitons produced in the 2D trap. See Fig. S1 for a sample superfluid image before the interaction quench.

Magnetic two-body interaction tuning. We control the atomic interaction by magnetic tuning the s-wave scattering length a near a broad cesium Feshbach resonance [32, 33]. We calibrate the magnetic field using microwave tomography after the 2D box loading. To obtain reliable magnetic field-to-scattering length conversion, we first identify the location for the scattering length zero-crossing ($a \approx 0 a_0$) near $B = 17 \text{ G}$. To do this, we slowly ramp down the background magnetic field (in 400 ms) from 18.6 G to a designated value to search for the minimum in the superfluid in-situ size as well as its expansion rate in a 2D time-of-flight. We identify the minimum occurs at $B = 17.120 \pm 0.006 \text{ G}$, which is consistent with the value $B = 17.119 \pm 0.001 \text{ G}$ measured using interaction-induced dephasing in Bloch oscillations [34]. We adopt the well-approximating formula used in Ref. [33] for the scattering length conversion

$$a(B) = (1722 + 1.52B/G) \left(1 - \frac{\Delta B}{B/G - B_0} \right), \quad (\text{A1})$$

where $\Delta B = 28.72$ and we have adjusted $B_0 = -11.60$ from its original value -11.74 to shift the zero-crossing in this formula to the calibrated value $B = 17.12 \text{ G}$. This shift results in less than 2 % change for scattering lengths far away from the zero-crossing, but is crucial for the scattering length conversion near $B = 17 \text{ G}$.

We convert the 3D scattering length a to the 2D interaction parameter using $g = \sqrt{8\pi a/l_z}$, where $l_z = 208 \text{ nm}$ is the vertical harmonic oscillator length. We confirm that this conversion remains valid for all the 2D samples explored, in which we have $l_z \gg |a|$ and finite initial density $n_i \gtrsim 5 \mu\text{m}^2$ with finite chemical potential $|\mu| \gg 0$ [35].

Soliton characterization

Fit routine to randomly distributed solitons. In order to characterize the size and the atom number in a soliton, we develop a non-linear least-squares fit routine to identify and fit random solitary density features with 2D Gaussians. To detect randomly distributed 2D solitons in a density image, we search for local density maxima above a threshold typically around $n \gtrsim 4 \mu\text{m}^2$ ($\sim 80 \%$ of the initial density n_i) using either the Laplacian of Gaussian method or a 2D maximum filter method. Following the peak detection, we then fit each local density maxima with a stretched 2D Gaussian, allowing the root-mean-square (r.m.s.) diameters along the major axes σ_x and σ_y and a rotated angle to vary independently. Additionally, we discard fit results that fail

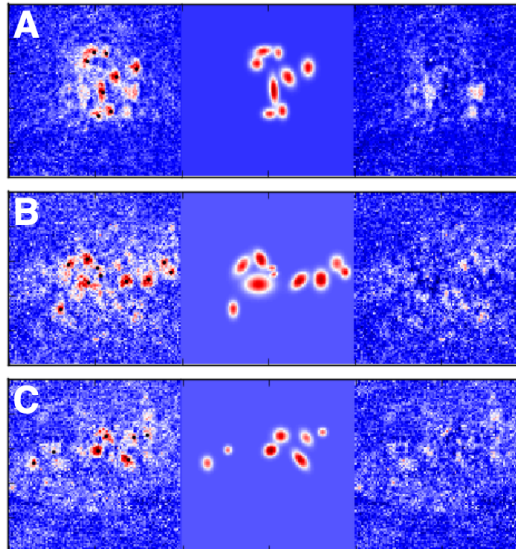


Fig. S2: Gaussian fits to single-shot sample images at $(g_f, \tau) = (\mathbf{A}) (-0.034, 42 \text{ ms})$, $(\mathbf{B}) (-0.019, 50 \text{ ms})$, and $(\mathbf{C}) (-0.019, 100 \text{ ms})$, respectively. Shown here are the density images (left images) with detected local maxima (marked by black dots), together with the 2D Gaussian fits (middle images) and the fit residuals (right images).

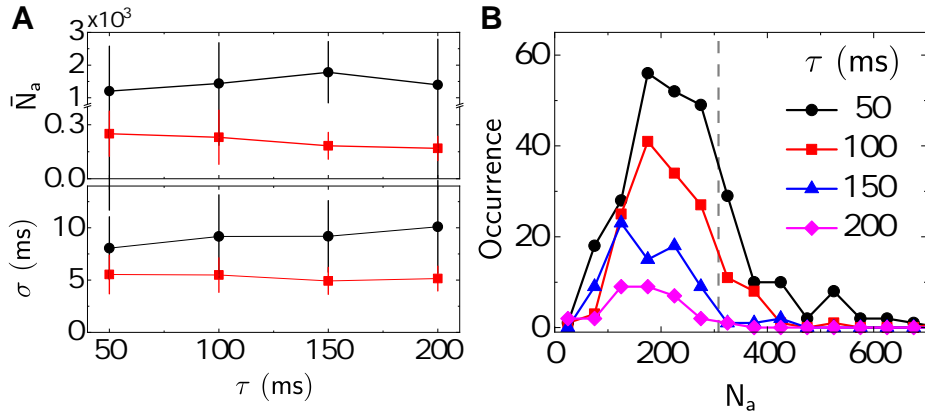


Fig. S3: (A) Mean soliton atom number \bar{N}_a and r.m.s. diameter σ versus hold time τ measured at $g_f = -0.004$ (black circles) and -0.019 (red squares), respectively. Error bars are standard deviations. (B) Occurrence of soliton atom number N_a at $g_f = -0.019$ and at the indicated hold time τ . Vertical dashed line marks the Townes threshold $N_{th} = 5.85/|g_f|$. Bin size is 50 .

to converge with fitted size variance below $0.2 \mu\text{m}^2$. This typically occurs when density blobs are too close to each other. In the main text, we present the geometric mean of the fitted size $\sigma = \sqrt{\sigma_x \sigma_y}$ and calculate fitted atom number as $N_a = \pi \sigma^2 A_{fit}/2$, where A_{fit} is the Gaussian amplitude. Due to the peak detection threshold and fit criterion, mean σ and \bar{N}_a presented in the main figures are primarily contributed by more isolated density blobs and by those with density n comparable to or bigger than the initial density n_i . See Fig. S2 for sample fit images.

Solitons at long hold time. Figure S3(A) illustrates two examples of fitted mean soliton size and atom number from images taken at long hold time $\tau \geq 50$ ms. A sample histogram of fitted atom number per soliton is plotted in Fig. S3 (B), from which the mean \bar{N}_a and the standard deviation δN_a (plotted as error bars) are evaluated. Fit results from measurements over a wide range of interaction g_f are plotted in Fig. 1 (C-D). From Fig. S3, we find no sign of rapid collapse or expansion following a single interaction quench. In Fig. S3 (B), the occurrence for all N_a reduces at longer hold time $\tau \geq 100$ ms due to secondary collapse as discussed in the main text.

Quench-induced dynamics in the density power spectrum

In a 2D gas with uniform mean density distribution, the density power spectrum at finite k is essentially the density static structure factor, which is the Fourier transform of the density-density correlation function [36]. In the following, we discuss the quench evolution of the structure factor (density power spectrum) measured in our samples.

Hyperbolic growth of density structure factor at short hold time after an interaction quench to $g_f < 0$. Immediately following the interaction quench, we expect density waves with wavenumber $0 < k < \sqrt{4|g_f|n_i}$ to grow unstably out of a Bose superfluid since the usual Bogoliubov dispersion becomes purely imaginary. There is no straightforward theory for evaluating quench evolution at all hold time. To gain insights, here we analytically evaluate the quench dynamics only in the very early stage when most of the atoms still remain in the zero momentum state. We focus on the time-evolution of the static structure factor [18, 37], that is, the density power spectrum measured in our quench experiment. Analytically, it can be evaluated as

$$S(\mathbf{k}) = \frac{1}{N} \sum_{\mathbf{q}, \mathbf{q}'} \langle \hat{a}_{\mathbf{q}+\mathbf{k}}^\dagger \hat{a}_{\mathbf{q}} \hat{a}_{\mathbf{q}'-\mathbf{k}}^\dagger \hat{a}_{\mathbf{q}'} \rangle, \quad (\text{A2})$$

where $\hat{a}_{\mathbf{k}}(\hat{a}_{\mathbf{k}}^\dagger)$ stands for the annihilation (creation) operator of a momentum state $|\mathbf{k}\rangle$. At very short hold time $\gamma\tau \ll 1$, where $\gamma = \frac{\hbar n_i |g_f|}{m}$, the Bose gas is still primarily populated by ground state atoms ($\hat{a}_0^{(\dagger)} \approx \sqrt{N}$), and the structure factor reduces to

$$S(\mathbf{k}) = \langle \hat{a}_{\mathbf{k}}^\dagger \hat{a}_{\mathbf{k}} \rangle + \langle \hat{a}_{-\mathbf{k}} \hat{a}_{-\mathbf{k}}^\dagger \rangle + \langle \hat{a}_{\mathbf{k}}^\dagger \hat{a}_{-\mathbf{k}}^\dagger \rangle + \langle \hat{a}_{-\mathbf{k}} \hat{a}_{\mathbf{k}} \rangle. \quad (\text{A3})$$

We perform the following transformation for momentum state within the range $0 < |\mathbf{k}| < \sqrt{4|g_f|n_i}$, expressing the momentum state operator with a set of bosonic mode operators $\hat{b}_{\mathbf{k}}$ ($\hat{b}_{-\mathbf{k}}^\dagger$) as

$$\begin{aligned}\hat{a}_{\mathbf{k}} &= i \left[u_k \hat{b}_{\mathbf{k}} + v_k \hat{b}_{-\mathbf{k}}^\dagger \right] \\ \hat{a}_{-\mathbf{k}}^\dagger &= -i \left[v_k \hat{b}_{\mathbf{k}} + u_k \hat{b}_{-\mathbf{k}}^\dagger \right].\end{aligned}\quad (\text{A4})$$

Here, we set the coefficients $u_k = \sqrt{\frac{\hbar\gamma}{2\epsilon(k)} + \frac{1}{2}}$ and $v_k = \sqrt{\frac{\hbar\gamma}{2\epsilon(k)} - \frac{1}{2}}$, $\epsilon(k) = \sqrt{|\epsilon_k^2 - 2\epsilon_k\hbar\gamma|}$ is the imaginary part of the Bogoliubov energy, $\epsilon_k = \frac{\hbar^2 k^2}{2m}$ is single particle dispersion, \hbar is the reduced Planck constant, and m is the atomic mass. $\hat{b}_{\mathbf{k}}$ ($\hat{b}_{-\mathbf{k}}^\dagger$) obeys the usual bosonic commutation relation. Using procedures similar to the standard Bogoliubov transformation, we can recast the weakly-interacting Hamiltonian into the following form

$$\hat{H} = \frac{N\mu}{2} + \sum_{\mathbf{k} \neq 0} \epsilon(k) (\hat{b}_{\mathbf{k}}^\dagger \hat{b}_{-\mathbf{k}}^\dagger + \hat{b}_{\mathbf{k}} \hat{b}_{-\mathbf{k}}) - \sum_{\mathbf{k} \neq 0} \left(\frac{\hbar^2 k^2}{2m} + \mu \right), \quad (\text{A5})$$

where the summation runs over half of momentum space and $\mu = -\hbar\gamma$ is the chemical potential. Note that, under this transformation, new excitations are generated (and also annihilated) in pairs as hold time increases. In the Heisenbeg picture, these operators obey a set of coupled equations of motion, $\dot{\hat{b}}_{\mathbf{k}} = \frac{i}{\hbar} [\hat{H}, \hat{b}_{\mathbf{k}}] = -\frac{i}{\hbar} \epsilon(k) \hat{b}_{-\mathbf{k}}^\dagger$ and its Hermitian conjugate, which lead to the following solution

$$\hat{b}_{\mathbf{k}} = \hat{b}_{0,\mathbf{k}} \cosh \frac{\epsilon(k)\tau}{\hbar} - i \hat{b}_{0,-\mathbf{k}}^\dagger \sinh \frac{\epsilon(k)\tau}{\hbar} \quad (\text{A6})$$

$$\hat{b}_{-\mathbf{k}}^\dagger = \hat{b}_{0,-\mathbf{k}}^\dagger \cosh \frac{\epsilon(k)\tau}{\hbar} + i \hat{b}_{0,\mathbf{k}} \sinh \frac{\epsilon(k)\tau}{\hbar}, \quad (\text{A7})$$

and $\hat{b}_{0,\mathbf{k}} (\hat{b}_{0,-\mathbf{k}}^\dagger)$ is the bosonic mode operator at time $\tau = 0$ right after the interaction quench. Plugging this solution into Eq. (A4) and evaluate the structure factor Eq. (A3), we then find the following time-dependent evolution

$$\begin{aligned}S(\mathbf{k}, \tau) &= \frac{\epsilon_k}{\epsilon(k)} \left[(\langle \hat{b}_{0,\mathbf{k}}^\dagger \hat{b}_{0,\mathbf{k}} \rangle + \langle \hat{b}_{0,-\mathbf{k}} \hat{b}_{0,-\mathbf{k}}^\dagger \rangle) \cosh 2\frac{\epsilon(k)\tau}{\hbar} \right. \\ &\quad \left. - (\langle \hat{b}_{0,\mathbf{k}}^\dagger \hat{b}_{0,-\mathbf{k}}^\dagger \rangle + \langle \hat{b}_{0,-\mathbf{k}} \hat{b}_{0,\mathbf{k}} \rangle) - i(\langle \hat{b}_{0,\mathbf{k}}^\dagger \hat{b}_{0,-\mathbf{k}}^\dagger \rangle - \langle \hat{b}_{0,-\mathbf{k}} \hat{b}_{0,\mathbf{k}} \rangle) \sinh 2\frac{\epsilon(k)\tau}{\hbar} \right].\end{aligned}\quad (\text{A8})$$

Here, the first line contains mode contributions that are seeded by the initial bosonic mode populations right after the quench. These modes grow ‘hyperbolically’ in the early stage of the quench dynamics. The second line contains the contributions from mode populations that are generated or annihilated from the interaction quench, where the hyperbolic term is expected to vanish, leaving only the constant term (see below).

Growing density waves from density fluctuations prior to the quench. By using Eq. (A4) and the Bogoliubov transformation, we can further relate the expectation values of the bosonic modes in Eq. (A8) to those of the phonon modes before the interaction quench. We find

$$\langle \hat{b}_{0,\mathbf{k}}^\dagger \hat{b}_{0,\mathbf{k}} \rangle + \langle \hat{b}_{0,-\mathbf{k}} \hat{b}_{0,-\mathbf{k}}^\dagger \rangle = \epsilon_k \frac{\hbar(\gamma_i + \gamma)}{\epsilon_i(k)\epsilon(k)} (\langle \hat{c}_{0,\mathbf{k}}^\dagger \hat{c}_{0,\mathbf{k}} \rangle + \langle \hat{c}_{0,-\mathbf{k}} \hat{c}_{0,-\mathbf{k}}^\dagger \rangle) \quad (\text{A9})$$

$$\langle \hat{b}_{0,\mathbf{k}}^\dagger \hat{b}_{0,-\mathbf{k}}^\dagger \rangle = \langle \hat{b}_{0,\mathbf{k}} \hat{b}_{0,-\mathbf{k}} \rangle = \frac{\epsilon_k^2 + \epsilon_k \hbar(\gamma_i - \gamma)}{2\epsilon_i(k)\epsilon(k)} (\langle \hat{c}_{0,\mathbf{k}}^\dagger \hat{c}_{0,\mathbf{k}} \rangle + \langle \hat{c}_{0,-\mathbf{k}} \hat{c}_{0,-\mathbf{k}}^\dagger \rangle), \quad (\text{A10})$$

where $\hat{c}_{0,\mathbf{k}} (\hat{c}_{0,\mathbf{k}}^\dagger)$ is the phonon annihilation (creation) operators, $\epsilon_i(k) = \sqrt{\epsilon_k^2 + 2\epsilon_k\hbar\gamma_i}$ is the Bogoliubov dispersion at interaction $g_i > 0$ prior to the quench, $\gamma_i = \frac{\hbar n_i g_i}{m}$, and we have used $\langle \hat{c}_{0,\mathbf{k}}^\dagger \hat{c}_{0,-\mathbf{k}}^\dagger \rangle = \langle \hat{c}_{0,\mathbf{k}} \hat{c}_{0,-\mathbf{k}} \rangle = 0$ in the above relation since there is no source or sink for phonons in our 2D gas. It is clear that the bosonic mode population Eqs. (A9-A10) is seeded by the initial thermal phonon population and zero-point fluctuations

$$\langle \hat{c}_{0,\mathbf{k}}^\dagger \hat{c}_{0,\mathbf{k}} \rangle + \langle \hat{c}_{0,-\mathbf{k}} \hat{c}_{0,-\mathbf{k}}^\dagger \rangle = \frac{2}{e^{\epsilon_i(k)/k_B T} - 1} + 1 = \coth \frac{\epsilon_i(k)}{2k_B T}. \quad (\text{A11})$$

Using the above relations and keeping only the wavenumber k -dependence, Eq. (A8) can now be simplified as

$$S(k, \tau) = S_0(k) \left[1 + \frac{2\epsilon_k \hbar(\gamma_i + \gamma)}{\epsilon(k)^2} \sinh^2 \frac{\epsilon(k)\tau}{\hbar} \right], \quad (\text{A12})$$

where the overall factor

$$S_0(k) = \frac{\hbar^2 k^2}{2m\epsilon_i(k)} \coth \frac{\epsilon_i(k)}{2k_B T} \quad (\text{A13})$$

is exactly the equilibrium static structure factor [38] right before the interaction quench (at $\tau = 0^-$).

Relationship with quench dynamics at $g_f > 0$. We note that the time-dependent density power spectrum Eq. (A12) is essentially the analytical continuation of quench-induced Sakharov oscillations in the structure factor at $g_f > 0$ [18],

$$S(k, \tau) = S_0(k) \left[1 + \frac{\epsilon_i(k)^2 - \epsilon^2(k)}{\epsilon(k)^2} \sin^2 \frac{\epsilon(k)\tau}{\hbar}, \right] \quad (\text{A14})$$

where now a coherent, sinusoidal oscillation in the structure factor replaces the hyperbolic growth. The calculation is in principle valid for all hold time τ for $g_f > 0$ provided no global trap scale or other effects set in, in contrast to the case of $g_f < 0$.

Universal scaling in the density power spectrum

Scaling at short hold time. The calculation in the previous section suggests that the density power spectrum exhibit a universal scaling behavior at short hold time. Focusing on the most unstable mode $k_p = \sqrt{2|g_f|n_i}$, where $\epsilon(k_p) = \hbar\gamma$, we expect the growth of density power spectrum $\tilde{S}(k_p, \tau) \equiv \frac{S(k_p, \tau)}{S(k_p, 0)}$ obey the following scaling relation

$$\mathcal{S}(\tilde{\tau}) = \zeta \left[\tilde{S}(k_p, \tilde{\tau}) - 1 \right], \quad (\text{A15})$$

where $\tilde{\tau} = \gamma\tau$ is the scaled time, ζ is a dimensionless amplitude scaling factor, and $\mathcal{S}(\tilde{\tau})$ is the scaled spectrum. Equation (A12) suggests a simple amplitude scaling factor

$$\zeta = \frac{\gamma}{\gamma + \gamma_i} \approx \frac{\gamma}{\gamma_i}, \quad (\text{A16})$$

where the approximation holds for $\gamma_i \gg \gamma$. The scaled spectrum should display a universal hyperbolic growth

$$\mathcal{S}(\tilde{\tau}) = 2 \sinh^2(\tilde{\tau}). \quad (\text{A17})$$

Approximate scaling at all hold time. There is no immediate theory extending the scaling relation at longer hold time $\tilde{\tau} \gtrsim 1$. However, our measured spectra surprisingly conform to the scaling form Eq. (A15) for an extended period of time. We have searched for the best amplitude scaling relation ζ for a larger time range, $0 < \tilde{\tau} < 5$. We find that the spectra scale the best with $\zeta \propto \gamma$, keeping explicit dependence on $n_i|g_f|$. We have similarly searched for an alternative scaling form $\mathcal{S}'(\tilde{\tau}) = \zeta S(k_p, \tilde{\tau})$, which again suggests a γ -dependent amplitude scaling factor; see Fig. S4. In the main text and in Fig. 2 (E), we adopt the best scaling form Eq. (A15) and a simple amplitude scaling factor in approximation of Eq. (A16),

$$\zeta = \frac{\gamma}{\bar{\gamma}_i}, \quad (\text{A18})$$

with mean $\bar{\gamma}_i = \hbar\bar{n}_i g_i/m = 306 \text{ s}^{-1}$ evaluated from all samples (mean $\bar{n}_i = 6/\mu\text{m}^2$ and standard deviation $\delta n_i = 1/\mu\text{m}^2$). We note that an alternative amplitude scaling $\zeta = \gamma/(\bar{\gamma}_i + \gamma)$ in reminiscence of the exact form Eq. (A16) gives a similar collapse.

For $\tilde{\tau} < 0.8$, the scaled spectrum suggests an approximate universal growth curve,

$$\mathcal{S}(\tilde{\tau}) \approx \alpha \sinh^2(\tilde{\tau}), \quad (\text{A19})$$

where $\alpha = 1.5(1)$ is obtained from a simple hyperbolic fit in Fig. 2 (E) for $0 < \tilde{\tau} < 0.5$. The hyperbolic growth is in agreement with the expectation from Eq. (A12). However, we obtain a smaller pre-factor $\alpha < 2$, likely due to effects such as depletion of ground state atoms, dissipation, or interaction between bosonic modes that are not considered in the simple analytical calculation.

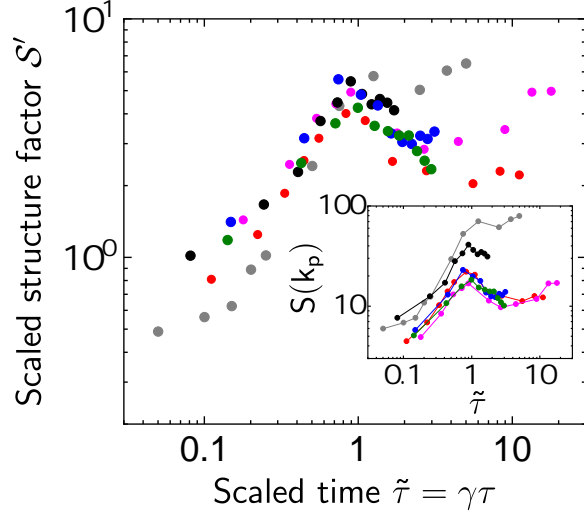


Fig. S4: An alternative scheme for rescaling the density power spectrum. Time-rescaled power spectra $S(k_p, \tilde{\tau})$ (inset) are derived from samples with $(g_f, n_i) = (-0.004, 4.3/\mu\text{m}^2)$ (gray), $(-0.011, 7.4/\mu\text{m}^2)$ (black), $(-0.019, 6.1/\mu\text{m}^2)$ (red), $(-0.027, 5.8/\mu\text{m}^2)$ (blue), $(-0.034, 5.4/\mu\text{m}^2)$ (magenta), and $(-0.034, 4.3/\mu\text{m}^2)$ (olive) as in Fig. 2. Each spectrum is amplitude-rescaled using the alternative scaling form $S'(\tilde{\tau}) = \frac{\gamma}{\gamma_i} S(k_p, \tilde{\tau})$. The spectrum at $g_f = -0.004$ is rescaled using $\gamma^* = 3.2\gamma$. The scaled spectra S' collapse near the peak at $\tilde{\tau} \approx 0.8$.

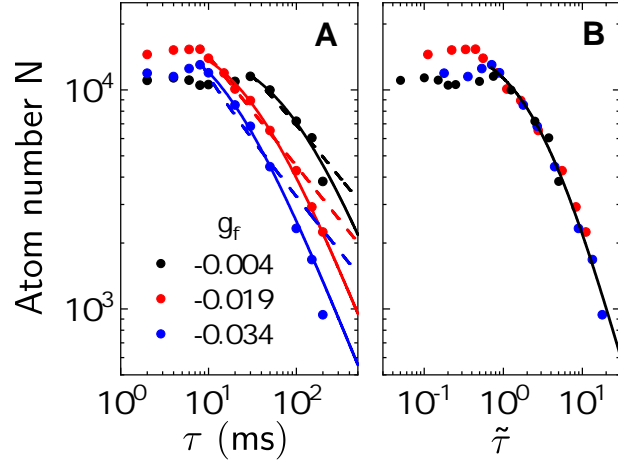


Fig. S5: Total atom number versus hold time τ and loss scaling. (A) Loss measurements at the indicated interactions g_f , as shown in Fig. 3. Solid lines (Dashed lines) are simple two-(three-)body loss fits using Eq. (A20). (B) Same measurements plotted in the scaled time $\tilde{\tau} = \gamma\tau$; for $g_f = -0.004$ (black circle), we have used $\gamma^* = 3.2\gamma$. Solid line is a fit using the generic model Eq. (A21) and the result is consistent with the two-body loss scaling; see text.

Universal 2D soliton binary collision dynamics

Fitting the total atom number loss. We discuss here the total atom number loss measurements as shown in Fig. 3 and their fits. The time dependence of the total atom number N is replotted in Fig. S5 together with analytical fits derived from the following simple rate equation

$$\frac{dN}{d\tau} = -\Gamma_{\text{dbody}} n N^{d-1}, \quad (\text{A20})$$

where $n = N/A$ is the surface number density, A is sample surface area (assumed constant), $d = 2$ or 3 gives two- or three-body loss scaling, respectively, and Γ_{dbody} is the corresponding rate coefficient. The fit begins at a time τ after loss initiates. As shown in Fig. S5, it is evident that the number decay scales faster than a three-body loss behavior and fits much better with a two-body loss model.

Determination of the universal loss scaling. To show the universal loss behavior, in Fig. S5 we alternatively rescale the time axis according to the interaction energy unit γ in each samples. For the measurement with $g_f = -0.004$, we rescale using $\gamma^* = 3.2\gamma$ as determined in Fig. 2. Although the initial atom number is quite different for individual samples, all measurements can approximately collapse onto one single curve at $\tilde{\tau} \gtrsim 0.8$, very similar to the observation reported in Ref. [25]. This timing, $\tilde{\tau}_i \approx 0.8$, also coincides with the critical time separating growth and decay in the universal density power spectrum in Fig. 2.

Taking the universal curve in Fig. S5, we determine the loss scaling. We fit the loss regime at $\tilde{\tau} > \tilde{\tau}_i$ with a generic loss model

$$N(\tilde{\tau}) = \frac{N(0)}{[1 + \tilde{\Gamma}(\tilde{\tau} - \tilde{\tau}_i)]^\lambda}, \quad (\text{A21})$$

using λ and $\tilde{\Gamma}$ as dimensionless fit parameters. We obtain $\lambda = 1.34 \pm 0.35$. If we use Eq. (A21) to fit individual loss curves in Fig. S5(B), we obtain mean $\lambda = 1.2 \pm 0.3$. All fitted λ are consistent with a two-body loss scaling $\lambda = 1$ and are far from a three-body loss behavior, which requires $\lambda = 0.5$. Fixing $\lambda = 1$, we obtain a universal rate coefficient $\tilde{\Gamma} = 0.45 \pm 0.04$ from the fit to the collapsed single curve.

Determination of the 2D binary collision coefficients Γ_s . In the main text, we reason that the effective two-body loss results from the binary collisions between solitons, which induce secondary collapse and create rapid atom loss. If this picture holds, we should have

$$\frac{dN_s}{d\tau} = -\Gamma_s n_s N_s, \quad (\text{A22})$$

where N_s is the number of solitons, $n_s = N_s/A$ is the surface density, and Γ_s is the 2D binary loss coefficient. Using $N_s = N/\bar{N}_a$ [25, 28] in Eq. (A22) and assuming \bar{N}_a is approximately constant over long hold time, we find the following simple relation

$$\Gamma_s = \Gamma_{\text{2body}} \bar{N}_a, \quad (\text{A23})$$

relating the measured rate coefficient Γ_{2body} to the binary collision coefficient Γ_s .

Universal scaling in Γ_s . We expect that the 2D binary collision coefficient $\Gamma_s \sim \sigma \bar{v}$ is proportional to the product of the linear cross-section $\sigma \approx \xi$ and the relative velocity between the solitons $\bar{v} \approx \sqrt{2}\hbar\pi/m\xi$. Their dependencies on the MI length scale ξ exactly cancel. This simple argument suggests

$$\Gamma_s = \eta \frac{\hbar\pi}{m} \quad (\text{A24})$$

is a universal number. Additional constant η should take into account the mean soliton loss per collision as merger only occurs when two solitons have like phases $\Delta\phi \approx 0$ [14]. Unlike in the 1D case, where neighboring solitons typically acquire opposite phase and are stable against collisions [4, 25, 26], we suspect $\sim 50\%$ probability for merger to occur. This gives an estimate

$$\eta \approx \sqrt{2}. \quad (\text{A25})$$

We note that the approximate collapse of loss curves in Fig. S5(B) already hints a universal collision coefficient. We can convert the universal rate coefficient $\tilde{\Gamma}$ to soliton collision coefficient and find

$$\Gamma_s = \bar{N}_a |g_f| \tilde{\Gamma} \frac{\hbar}{m}, \quad (\text{A26})$$

suggesting that if $\bar{N}_a |g_f|$ is a universal number then so is Γ_s , and vice versa. From measured $(\tilde{\Gamma}, \bar{N}_a |g_f|) = (0.45 \pm 0.04, 6 \pm 1)$, we obtain $\eta = 0.9 \pm 0.2$.

Independent determination of η . The universal constant η can also be determined using the observed linear scaling of $\Gamma_{2\text{body}}/|g_f| = 3.9 \pm 0.6 \times 10^{-6} \text{ cm}^2/\text{s}$ in Fig. 3. Plugging the fitted slope into Eq. (A23) with experimentally determined $\bar{N}_a|g_f| = 6 \pm 1$ (Fig. 1), we find $\eta = 1.6 \pm 0.4$ in very good agreement with the simple expectation Eq. (A25).

Furthermore, without any assumption on scaling or universal number, individual data points in Fig. 3(B) have also been converted to Γ_s in Fig. 3(C), using all experimentally measured values ($\Gamma_{2\text{body}}, \bar{N}_a$) at three different $|g_f|$. The converted results all conform with the prediction Eq. (A24), giving a mean $\eta = 1.9 \pm 0.7$.

Collision lifetime of solitons. Following the determination of universal collision dynamics, we also obtain the collision lifetime of solitons right after wave collapse and soliton formation near $\tilde{\tau} \approx \tilde{\tau}_i$. We calculate the lifetime

$$\Delta\tau_s = \frac{1}{\Gamma_s n_s} \approx \frac{m\bar{N}_a}{\eta\pi\hbar n_i} \approx \gamma^{-1}, \quad (\text{A27})$$

where we have used $n_s = n_i/\bar{N}_a$, the measured universal threshold $\bar{N}_a|g_f| = 6$, and $\eta = 1.9$.

Fitting soliton collapse following the second interaction quench

Following the second interaction quench in path (ii) as shown in Fig. 4, initial soliton number $\bar{N}_a(\tau_2 = 0)$ exceeds the new Townes threshold by three-fold and solitons begin to collapse. Both the soliton size σ and mean atom number \bar{N}_a reduces. The atom number loss within a soliton is due to three-body recombination that is still 3D in nature. To quantify the three-body loss rate, we develop an effective loss fit that takes into account the shrinking soliton size. In addition, we assume that binary collision between solitons does not interfere with the collapse dynamics within a soliton, which likely occur concurrently.

First, from the linear fit in Fig. 4(B), we obtain the linear time dependence $\sigma(\tau_2) = \sigma_0 + \dot{\sigma}\tau_2$, where $\sigma_0 = 8.0 \mu\text{m}$ and $\dot{\sigma} = -0.11 \text{ mm/s}$. We then plug this into standard three-body recombination loss model and obtain

$$\begin{aligned} \frac{d\bar{N}_a}{d\tau_2} &= -\frac{L_3}{3!} \langle n_{3\text{D}}^2 \rangle \bar{N}_a \\ &= -\frac{L_3}{9\sqrt{3}\pi^3\sigma(\tau_2)^4 l_z^2} \bar{N}_a^3, \end{aligned} \quad (\text{A28})$$

where L_3 is the three-body loss coefficient. We have used a Gaussian form for the soliton 3D density

$$n_{3\text{D}}(x, y, z) = \frac{4\bar{N}_a}{(2\pi)^{3/2}\sigma^2 l_z} e^{-\frac{2x^2}{\sigma_x^2} - \frac{2y^2}{\sigma_y^2} - \frac{z^2}{2l_z^2}}, \quad (\text{A29})$$

where $\sigma = \sqrt{\sigma_x\sigma_y}$ is the geometric mean of the r.m.s. diameters along the horizontal (x, y) axes. From the above equations and the approximate linear time-dependence in σ , we derive an analytical fit formula

$$\bar{N}_a(\tau_2) = \frac{\bar{N}_a(0)}{\sqrt{1 + \frac{2L_3\bar{N}_a(0)^2}{27\sqrt{3}\pi^3 l_z^2 |\dot{\sigma}|} \left[\frac{1}{(\sigma_0 + \dot{\sigma}\tau_2)^3} - \frac{1}{\sigma_0^3} \right]}}, \quad (\text{A30})$$

where L_3 is the fit parameter. This effective three-body loss model captures very well the loss curve except beyond $\tau_2 > 36 \text{ ms}$ when the atom number reaches the new Townes threshold. Fitting measured $\bar{N}_a(\tau_2)$ in the range $\tau_2 = 0 \sim 36 \text{ ms}$, we obtain $L_3 = 1.1 \pm 0.1 \times 10^{-23} \text{ cm}^6/\text{s}$, which is five orders of magnitude higher than the 3D thermal gas measurements $L_3 \sim 10^{-28} \text{ cm}^6/\text{s}$ with similar scattering lengths [33].